A Large Ensemble Simulation of Geomagnetic Storms – Can Simulations Predict Ground Magnetometer Station Observations of Magnetic Field Perturbations?

Q. Al Shidi[1], T. Pulkkinen[1], G. Toth[1], A. Brenner[1], S. Zou[1], J. Gjerloev[2]

[1]Climate and Space Sciences and Engineering, University of Michigan
[2]John Hopkins University - Applied Physics Laboratory

Key Points:

- SWMF simulations were carried out for 122 geomagnetic storms during 2010 and 2019.
- SWMF simulations of ground magnetic disturbances provide results comparable to those of geomagnetic indices.
- Simulation performance for high-latitude magnetic perturbations requires accurate modeling of the magnetosphere-ionosphere coupling.

Corresponding author: Qusai Al Shidi, `qusai@umich.edu`

Abstract

We use the Space Weather Modeling Framework (SWMF) Geospace configuration to simulate a total of 122 storms from the period 2010-2019. With the focus on the storm main phase, each storm period was run for 54 hours starting from 6 hours prior to the start of the Dst depression. The simulation output of ground magnetic variations were compared with ground magnetometer station data provided by SuperMAG to statistically assess the Geospace model regional prediction performance. Our results show that the regional predictions at mid-latitudes are quite accurate, but the high-latitude regional disturbances are still difficult to predict due to the complexity of the magnetosphere – ionosphere coupling processes.

Plain Language Summary

Ground magnetic disturbances can cause spurious currents in power networks, natural gas pipelines, or other systems, and hence are a key target of space weather predictions. The ground magnetic disturbances produced by currents flowing in the ionosphere around 100km as well as currents at higher altitudes. These currents are powered by complex processes related to the solar wind plasma and magnetic field interaction with the Earth's space environment. We use a large-scale simulation of the Earth's space environment together with measurements of the ground magnetic field variations from over 100 stations around the world to statistically assess the model performance. Our results indicate that at the mid-latitudes (e.g. over the continental U.S.), the model performance is quite good even in regional scale, but at high latitudes near the arctic circle, the model performance is not as good due to the complexity of the auroral processes influencing the local ionospheric currents creating highly localized and strong magnetic perturbations.

1 Introduction

The Earth's surface magnetic field varies in response to currents in the near-Earth space (Chapman & Bartels, 1941) and in the ionosphere (Zmuda & Armstrong, 1974). The ground signal from the high-altitude currents is dominated by the ring current, but during geomagnetic storms, the magnetopause compression especially at the storm onset can cause substantial disturbances due to enhanced dayside magnetopause currents (Villante & Piersanti, 2008), while the tail currents can significantly contribute to the signal during the storm main and recovery phases (Ganushkina et al., 2010). The high-altitude currents are best detected by sub-auroral magnetometers where there are no ionospheric currents overhead, and thus the H (magnitude horizontal to the ground) component of the magnetic field provides a measure of the intensity of the current flowing parallel to the equatorial plane (Huang et al., 2004). At the auroral latitudes, the signal is dominated by the ionospheric currents at about 100-km altitude (Richmond et al., 1990).

Geomagnetic indices are used as a measure of the level of geomagnetic activity. The stormtime disturbance index Dst, and its high-cadence in time version SYM-H record the average of the magnetic variation at four and six mid-latitude stations respectively around the Earth, weighted by the average of the station colatitudes (Sugiura & Poros, 1971). The Dst is used as a measure of storm intensity, and is often interpreted as being proportional to the intensity of the ring current encircling the Earth (Siscoe & Crooker, 1974). The Auroral Electrojet indices are composed of 12 high-latitude (northern hemisphere) stations as extrema of the north components at the stations at each time step. Thus, the auroral upper (AU) index is a measure of the peak eastward current in the ionosphere, while the auroral lower (AL) index is proportional to the peak westward current (Davis & Sugiura, 1966).

Rapid variations in the geomagnetic field induce a geoelectric field at the Earth's surface, which in turn drive Geomagnetically induced currents (GIC), which can have harmful effects in power grids, natural gas pipelines, or other technological systems (Pirjola et al., 2000). The geoelectric field depends on the ground conductivity structure, which means that the local geology influences the formation and intensity of the GIC (Zheng et al., 2013). As the power spectrum of the geoelectric field is dominated by frequencies below 1 Hz, the GICs act as a direct current (DC) component on top of the 50 or 60 Hz alternating current (AC) power system (Pulkkinen et al., 2017). The effects in the power systems include saturation of transformers, which can generate equipment damage and/or system-wide disturbances and power outages (Bolduc, 2002; Lanzerotti, 2001). In the natural gas pipelines, the DC currents can cause corrosion and thus shorten the lifetime of the system (Boteler et al., 1998; Pirjola et al., 2005). As the GIC and their effects on the systems depend on the regional rather than global level of disturbances, the global activity indices are not best suited for serving the system operators wishing to get advance warnings and nowcasts of the intensity of the disturbances (Abt Associates Inc., 2019). The Federal Emergency Management Agency National Threat and Hazard Identification and Risk Assessment report (Federal Emergency Management Agency, 2019) recognized space weather-associated power outage as one of two hazards (besides a pandemic) that can have nation-wide impacts. Furthermore, the Promoting Research and Observations of Space Weather to Improve the Forecasting of Tomorrow Act, or the PROSWIFT Act, (Congress, 2020) recognizes addressing the GIC risk to power systems as critical for the nation's safety and security.

The NOAA Space Weather Prediction Center (SWPC) in Boulder, CO, produces ground magnetic perturbation maps based on the University of Michigan Space Weather Modeling Framework (SWMF) Geospace model for the ground infrastructure operators (Space Weather Prediction Center, 1960). This study addresses the capability of the SWMF Geospace to provide accurate regional predictions of the ground geomagentic disturbances. While the Geospace performance has been comprehensively assessed with regard to the global indices (Cash et al., 2018; Liemohn et al., 2018), the knowledge of the model performance at the level of individual station comparisons remains anecdotal. In this paper we describe a statistical database of storm simulations and use that together with the SuperMAG ground magnetometer observations to assess the model performance at individual stations, comparing results from different latitude bands. Section 2 describes the methodology, Section 3 presents the results, Section 4 summarizes the results and concludes with discussion.

2 Methodology

2.1 Observations

Following the often-used definition of a geomagnetic storm as an event with a peak Dst value below -50 nT, we examined all periods during 2010–2019 fulfilling that condition. A small subset of the periods were discarded due to lack of clear signature of storm onset or main phase development or significant data gaps in solar wind and IMF records. A total of 122 such periods with SYM-H minimum below -50 nT were included in the study. The storm onset time was selected to be the time when the SYM-H index started to decrease (often following a compression caused by the ICME-associated shock). Each interval had a duration of 54 hours starting from 6 hours prior to the storm onset. While this limitation captures all storm main phases in the dataset, it does not always extend far enough to capture the entire storm recovery phase.

The solar wind measurements were obtained from the OMNI database (Goddard Space Flight Center, 2021), which provides the interplanetary magnetic field (IMF) and the solar wind plasma parameters propagated to the upstream bow shock allowing for direct association with the geomagnetic activity indices (Papitashvili et al., 2014). The solar wind driver intensity was assessed using the Newell coupling parameter (Newell et al., 2007), which is proportional to the rate of change of magnetic flux at the nose of the magnetopause, and can be written in the form

$$\frac{d\Phi_{MP}}{dt} = \alpha \left[\left(\frac{V}{1\,\mathrm{km/s}} \right)^2 \frac{B_T}{1\,\mathrm{nT}} \sin^4 \frac{\theta}{2} \right]^{2/3} \tag{1}$$

where $\theta = \tan^{-1}(B_Y/B_Z)$ is the IMF clock angle and $B_T = (B_Y^2 + B_Z^2)^{1/2}$ denotes the transverse component of the magnetic field perpendicular to the Sun-Earth line, and α is a scaling factor of the order of 10^3 (Cai & Clauer, 2013). The ground magnetic field variations were analyzed using the SuperMAG (Gjerloev, 2012) database comprising 1-min magnetic measurements from several hundred magnetic stations over the globe through the INTERMAGNET et al. (2021) network. While the total number of stations is large, at any given time instance, the number of available stations ranges from about 50 to 150. For each event, we used all stations that had continuous data throughout the event interval.

Figure 1 illustrates a sample storm in the data set. The major storm occurred on February 18-20, 2014, and had a peak SYM-H intensity below -100 nT. The panels show the Newell coupling function illustrating the solar wind driving intensity, the SYM-H index, the AL index, and the Cross-Polar Cap Potential (CPCP) estimated using a model driven by solar wind parameters and the Polar Cap Index (PCI) (A. J. Ridley & Kihn, 2004). As an example, the two bottom panels show observations from two stations, from Boulder, Colorado, in the mid-latitudes, and from Yellowknife, Northwest Territories, Canada, within the auroral region (note that the observations are shown in different scales).

2.2 Space Weather Modeling Framework Geospace Configuration

The Space Weather Modeling Framework (SWMF) is a combination of numerical models to simulate space physics processes from the Sun to the Earth's upper atmosphere and outer heliosphere (Tóth et al., 2012; Gombosi, Tamas I. et al., 2021). The core of the SWMF is the Block-Adaptive-Tree-Solarwind-Roe-Upwind-Scheme (BATS-R-US), a 3D model solving the magnetohydrodynamic equations. The Ridley Ionosphere Model (RIM) is a potential field solver for the ionosphere, and the Rice Convection Model (RCM) is a kinetic model of the ring currrent and inner magnetosphere. The SWMF couplers tie these three components together to simulate the space weather effects in space and on ground. The Geospace configuration used for this study mimics the one operationally used at the NOAA Space Weather Prediction Center (SWPC).

The solar wind and the magnetosphere are modeled by BATS-R-US in ideal MHD mode with the adaptive grid resolution changing between $0.125\,R_E$ in the near-Earth region and $8R_E$ in the distant tail. The simulation box in the Geocentric Solar Magnetospheric (GSM) coordinates covers the region from $32\,R_E$ to $-224\,R_E$ in the X direction and $\pm128\,R_E$ in the Y and Z directions. The inner boundary is a spherical surface at radial distance $R = 2.5\,R_E$.

The RIM model solves the Poisson equation for the electrostatic potential at a two-dimensional ionospheric surface (A. Ridley et al., 2006). BATS-R-US feeds the RIM the field-aligned currents from the simulation inner boundary, and the ionospheric conductances are derived using the incoming field-aligned current intensity and location combined with background dayside and night-side conductances. The potential is set to zero at the lower latitude boundary at 10°. The RIM then solves the Vasyliunas (1970) equation for the electric potential, and gives the velocity boundary condition by feeding the electric field values back to the MHD simulation. The ionosphere and magnetosphere models are coupled at a cadence of 5 seconds.

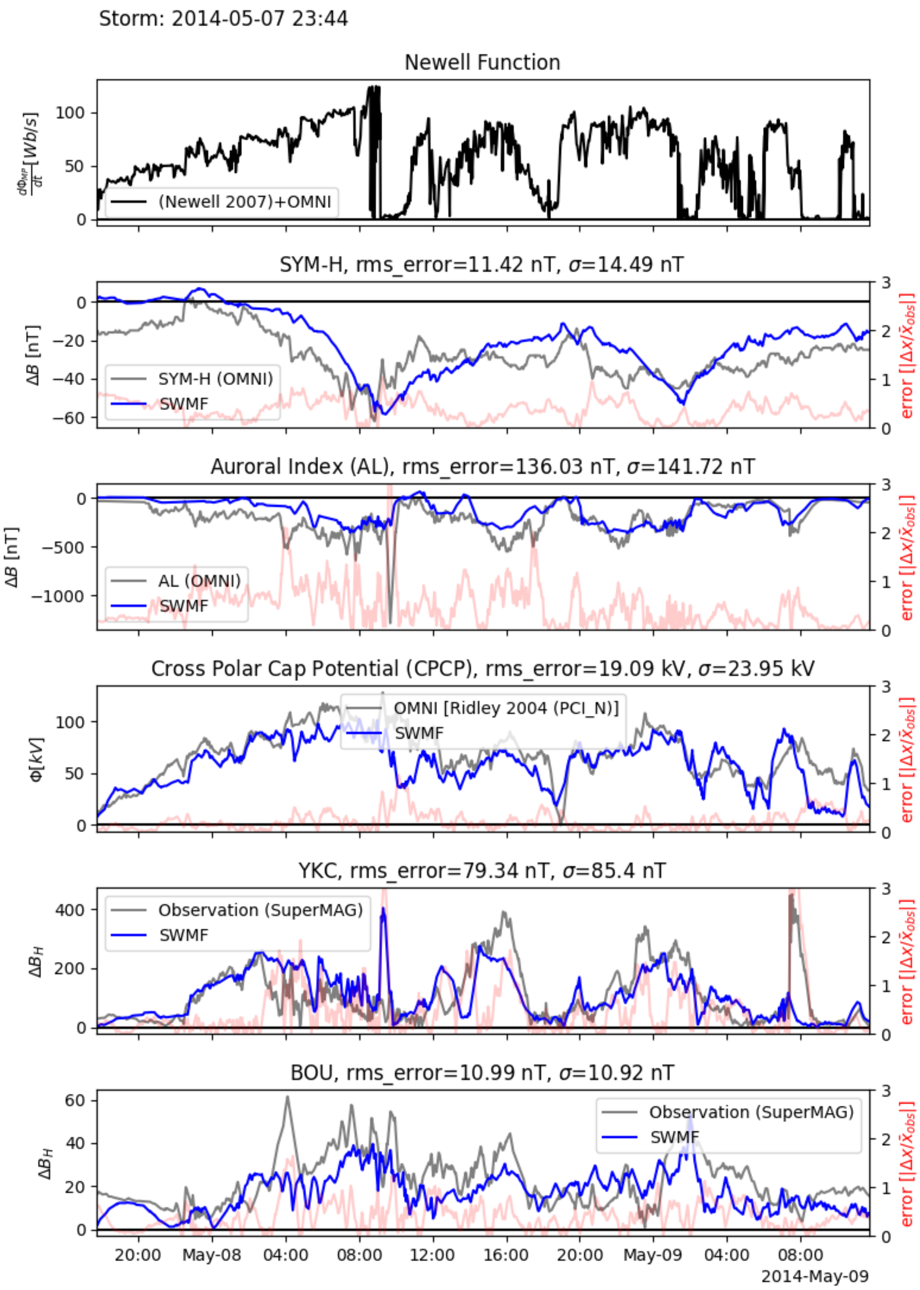

Figure 1. A sample storm on May 7-9, 2014. From top to bottom: The Newell et al. (2007) function, the SYM-H index, the AL index, the CPCP using the A. J. Ridley and Kihn (2004) model, magnetic north components from Yellowstone, Canada and Boulder, CO. Observed values are shown in black, while the Geospace simulation results are shown in blue. The red lines show the error normalized to the mean of the observed values (error = (observed-model)/mean(observed)). For each panel, the root mean square (rms) error and standard deviation (σ) are given in the caption.

The ground magnetic disturbances predicted by the simulation are computed by Biot-Savart integration of the currents external to the Earth, using both the BATS-R-US (for the magnetospheric currents) and RIM (for the ionospheric currents) models (Yu & Ridley, 2008). The values are then rotated to obtain the B_{North}, B_{East} and B_{Down} components used by the ground magnetic stations. The model output contains a regular 360×180 grid of magnetic disturbances between 0–360° longitude and ±90° latitude. The simulated ground magnetic field disturbances were stored at 1-minute cadence.

Figure 1 shows the simulated values (in blue) over the observed values as well as the difference between the observed and simulated values normalized by the mean (red, scale to the right). While the simulated SYM-H follows the observed one quite well, it can be seen that the AL index is not as well reproduced by the simulation: the simulated AL follows the observations early in the storm when the AL is not very large, but the simulation does not catch the very strong currents associated with the substorm activity near the peak of the storm. This is typical of the simulations in the data set. The two bottom panels show representative local magnetic measurements from YKC and BOU. In both latitude bands, the simulation tends to underestimate the magnitude of the disturbance.

2.3 Statistical Storm Simulation Dataset

The full dataset (Al Shidi, 2022) comprises 122 storms during years 2010–2019. Figure 2 shows the individual events as well as the superposed epoch results for the observed and simulated SYM-H as well as for the error computed as the difference between the observed and simulation values in 1-min temporal resolution. It is clear that the superposed epoch curves follow each other very well, and the superposed epoch error is quite small, while showing a trend toward negative errors (model values recovering faster than the observed ones). Although not shown here, this negative trend is largely caused by large storms with maxima below −100 nT. It is also notable that the scatter of the errors is larger during the storm main phase and reduces toward the storm recovery. This is indicative of the highly varying SYM-H values that can lead to large errors e.g. by a small time shift between the model and the simulation. The storms included in the study are shown in the appendix.

3 Results

3.1 Error Statistics

The one-minute-data from the the simulation at the virtual station locations were compared with the minute-data from the available SuperMAG stations during 48 hours of the simulation following the storm onset. The errors were calculated as a simple difference

$$\text{Error}(\mathbf{\Delta B}) = \mathbf{\Delta B}_{\text{SuperMAG}} - \mathbf{\Delta B}_{\text{SWMF}}, \tag{2}$$

which produces negative error values when the simulation shows lower activity (less negative values) than the observations (i.e., underestimates the disturbance intensity), and positive error values when the simulation overestimates the (negative) disturbance intensity.

The left panels of Figure 3 show the distribution of errors in all three magnetic components (North, East, Down) averaged over all simulated storms for two representative stations, Yellowknife (YKC) at the auroral latitudes and Boulder (BOU) in the mid-latitudes. The gray-shaded region in the figures indicates the values between the mean of the negative and mean of the positive values. (Note that the two stations are shown in different horizontal scale).

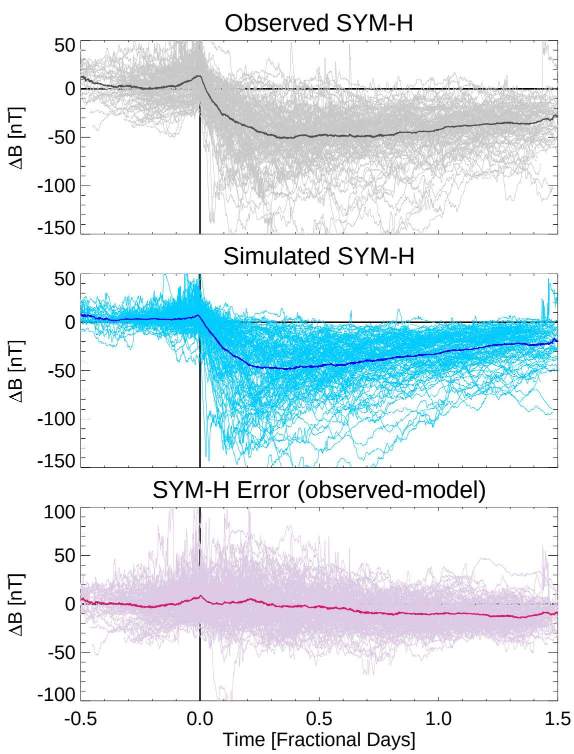

Figure 2. Superposed Epoch analysis of the simulated 122 storms. The panels show (top) observed SYM-H, (middle) simulated SYM-H, and (bottom) error in SYM-H defined as the difference Observed - Model values. The dark curves show the superposed epoch values using start of Dst decrease as zero epoch.

The error statistics has roughly a normal distribution. The Fisher-Pearson skewness coefficient values also shown in the figures show that the errors mostly fall in the category of nearly symmetric ($|g_1| < 0.5$) or moderately skewed ($0.5 < |g_1| < 1$) distributions. However, there is a systematic tendency for the mean of the negative values to be larger (in absolute values) than the mean of the positive values, indicating that there is a longer tail in the negative error distribution or in the degree of underestimation of the disturbance magnitude.

The error magnitude differences between a mid-latitude and auroral station reflects the different drivers and magnitudes of the disturbances: Under most conditions, the mid-latitude stations record the variations in the ring current, with typical signal intensity of few tens of nT, or during storm times up to -100 nT and even below. Other currents that contribute are the magnetopause current and field-aligned currents (Ganushkina et al., 2018). On the other hand, the auroral stations recording the strong substorm activity, the disturbances are of the order of several hundred nT, at times reaching to -1000 nT and even more.

The right panels of Figure 3 show the error statistics for all stations in the latitude band above 50° magnetic latitude in both northern and southern hemispheres (top panel) and in the latitude band $-50° < \text{Mlat} < 50°$, representative of auroral/polar cap stations and mid/low latitude stations, respectively. While the distributions are slightly wider than those for individual stations, they share the same features of relatively symmetric distributions with long tails in the negative error direction.

3.2 Error Statistics at Individual Stations

Next we examine the errors at individual stations, to resolve the spatial distribution of the errors over the globe. To that end, we examine the horizontal magnetic field component B_H given as

$$B_{\text{Horizontal}} = \sqrt{B_{\text{North}}^2 + B_{\text{East}}^2}, \tag{3}$$

which always gives a positive signal. In this case, positive errors mean that the model underestimates the disturbance intensity, while negative errors mean model predicting larger than observed signal. The horizontal component including the Eastward component records also currents that are not strictly in the east-west direction (high latitudes) or along a symmetric torus (mid-latitude stations).

Figure 4 gives a geographical map of the median error of the horizontal component. Consistent with the overall average, the errors are smaller for the lower-latitude stations and larger for the higher-latitude stations. The errors are largest at stations poleward of the auroral oval, within the region typically in the open field-line polar cap region.

Figure 5 shows the median errors for all available magnetic stations (crosses) together with the standard deviation of values above and below the median (vertical bars). The four plots show the North and Horizontal components, and the two latitude bands above and below 50° separately. The top panels showing the northern high-latitude stations show the typical auroral region with gray shading for reference.

The top panels show that the median errors are quite small even in the high latitude region, but the medians tend toward larger negative values (model underpredicting of the observed values) within the polar cap. Similar trend is not seen in the horizontal component, which indicates that there is a consistent rotation of the horizontal magnetic field between the model and the observations, but that the observed horizontal field magnitude on average is quite accurately predicted by the model.

The standard deviations of the errors are largest around the auroral region, with the standard deviations larger in the direction of model underpredicting the observed disturbance magnitude. This reflects the model tendency to miss strong auroral latitude

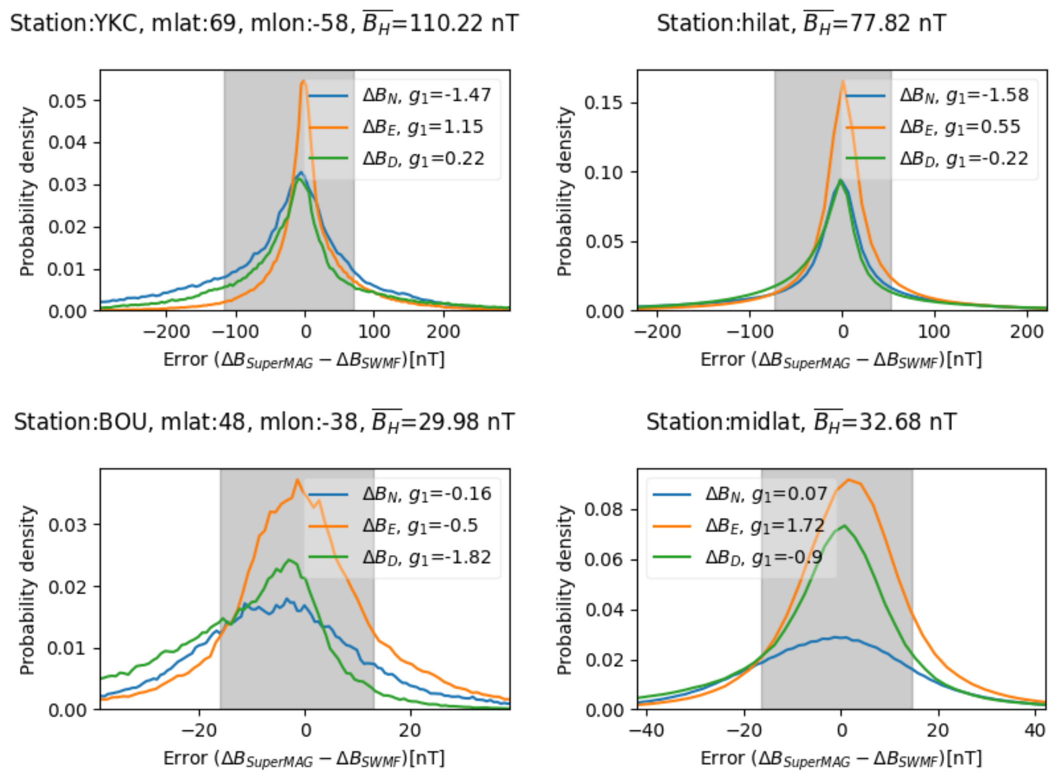

Figure 3. Left panels: Error distributions for magnetometer station in Yellowknife, Canada (top) and Boulder, Colorado (bottom) Right panels: Error distributions for stations in the high-latitudes (50–90° magnetic latitude, top), and mid-latitudes (-50–50° magnetic latitude, bottom). The grey shading limits the values between the mean of the negative and positive values. All three magnetic field components are shown: North (blue), East (orange), and Downward (green). The Fisher-Pearson skewness values (g_1) for each component are given in the legend.

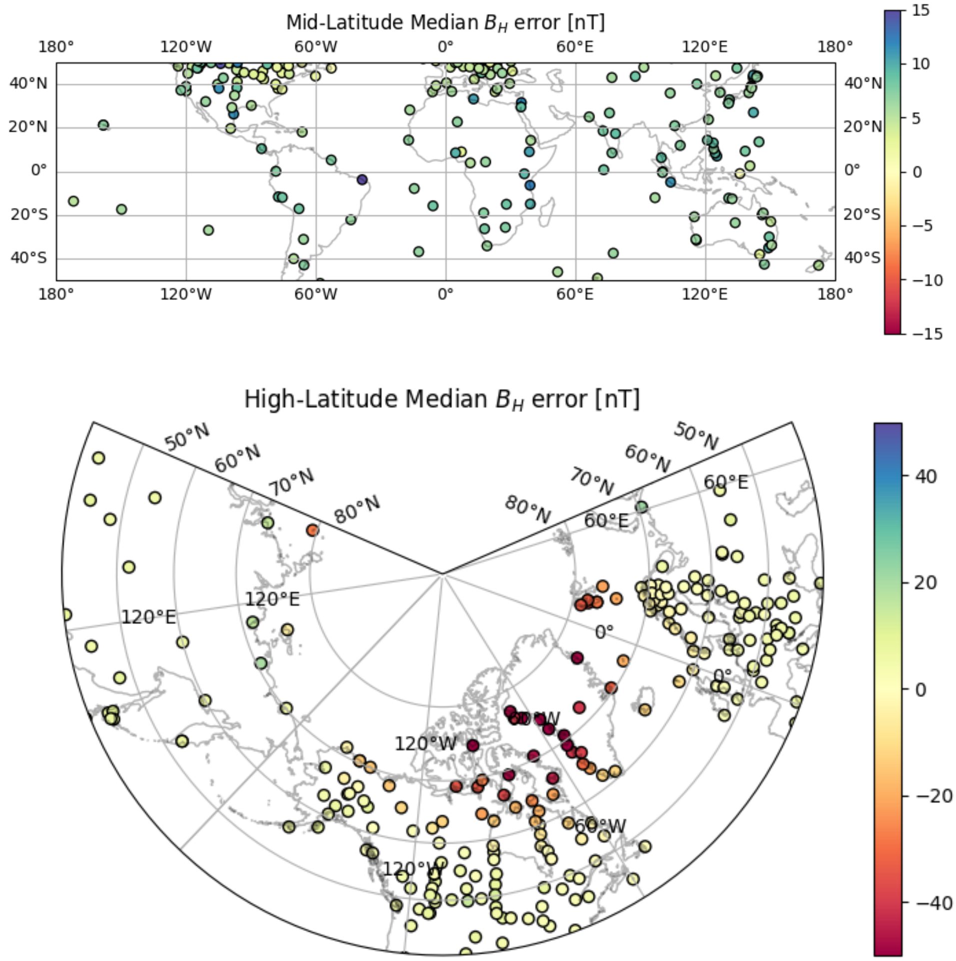

Figure 4. Geographical map of station median horizontal magnetic field component errors. The color scale shows values under-predicted by the model in blue colors, and values over-predicted by the model in red colors.

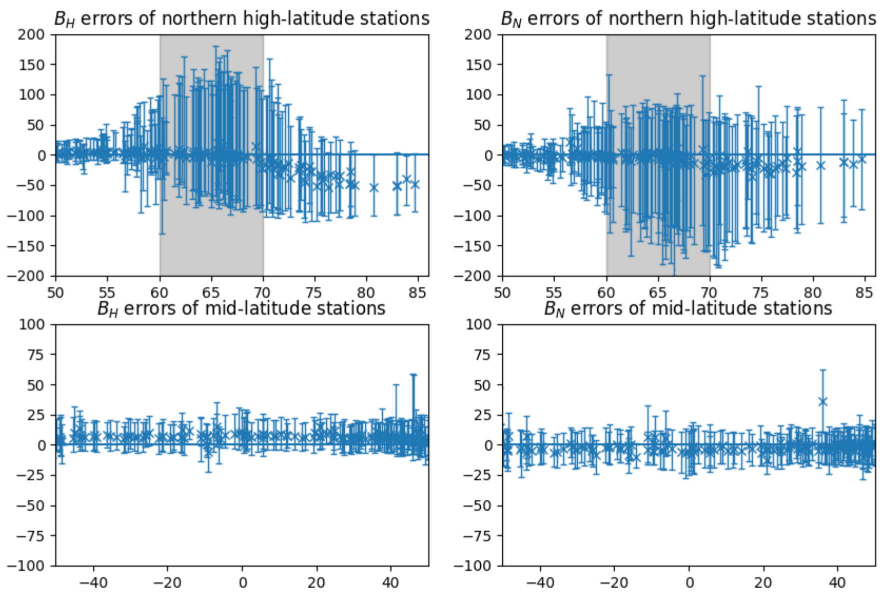

Figure 5. From top to bottom, horizontal component errors in high-latitudes (50°–90° magnetic latitude) and mid-latitude (-50°–50° magnetic latitude) of individual magnetometer stations. The crosses show the median error while the error bars show the standard deviation above and below the median. In the top panels, the grey-shaded regions show the typical auroral zones.

activity associated with substorms and other magnetospohere – ionosphere coupling processes.

The bottom panels depicting the lower-latitude observations show that the median errors are typically in the direction of slight underprediction, and the standard deviations are similarly skewed. The error distributions are relatively constant over all latitudes. The similarity of the distributions at all stations is indicative of the consistent capability of the simulation as well as the high quality of the data with only a few stations with spurious results. There are a few stations located near the magnetic equator that show more undpredicted results. This could be due to euqatorial electrojets that are not represented in the simulation (Forbes, 1981; Rastogi, 1989; Onwumechili, 2019).

3.3 Heidke Skill Score Analysis

To quantify the ability to forecast measurements at the individual stations, we assign Heidke skill score values (HSS) (Heidke, 1926) to each station. The Heidke Skill score is defined in the typical skill score format with skill given by the ratio of the difference between score and the score for chance to the difference between the perfect score and score for chance. The HSS can be obtained through a 2×2 contingency table where the simulation and observations are compared to a threshold value (Table 1), and obtained using the definition (Jolliffe & Stephenson, 2012)

$$\mathrm{HSS} = \frac{2(H \cdot N - M \cdot F)}{(H+M)(M+N)+(H+F)(F+N)}, \tag{4}$$

Table 1. 2×2 contingency table describing the HSS. "Above" and "Below" indicate field values above and below the threshold.

	Station above	Station below
Simulation above	H (hit)	F (false positive)
Simulation below	M (miss)	N (true negative)

which shows that the HSS maximum value for no misses and no false positives is 1, value of zero indicates no skill, and negative values indicate skill worse than chance.

A key for the usability of the HSS to assess the prediction quality for operational customers lies in a correct selection of the threshold value separating "Hits" (Events) and "True negatives" (Quiet time). As the typical signal intensity varies with latitude, the thresholds for "Events" should likely be different for stations at different latitudes.

For the lower latitude stations, the storm limit -50 nT can be argued to be a suitable event threshold. In this database consisting of simulations of storm periods, reaching below the 50 nT threshold should occur for a substantial portion of the time, and such disturbances are likely to drive currents that are of concern e.g. to the power system operators.

Figure 6 shows a geographic map of the HSS values for each of the stations available through the SuperMAG network using the 50 nT event threshold. The skill scores vary from very low (especially in the polar regions) to above 0.6, with best HSS values at the low and mid-latitudes.

Interestingly, there is a band of lower skill scores in the range 0.3–0.4 in the latitude band around 50-60° latitude. This may be due to the fact that during storms, this latitude band is often underneath the ionospheric currents, which create very strong disturbances. If the model auroral oval is not able to accurately track the real one, motion of the equatorward edge can cause the station to be on one side of the boundary in the model and on the other side in the simulation.

Note that the skill scores with the 50 nT threshold are quite good in the auroral oval region around 60°–70° geographic latitude. This indicates a high number of hits, highlighting the fact that the model – even if not capturing the intensity of the perturbations – is often able to capture the event occurrence.

The bottom panel of Figure 6 shows the HSS results with a threshold of 200 nT more corresponding to the magnitude of the auroral electrojet currents. Obviously, the skill scores at lower latitudes are low, as the disturbances rarely reach such high values. The auroral oval region shows a strong agreement, HSS values of 0.5–0.7, if the threshold is set to 200nT. The threshold of 200 nT was chosen as it is a typical value signifying auroral currents (Klumpar, 1979; Akasofu et al., 1980; Waters et al., 2001).

4 Discussion

In this paper, we have addressed the capability of the SWMF Geospace model to predict magnetic disturbances at individual stations. In general, the results are encouraging with positive HSS skill scores in the range of 0.3–0.6 for most stations.

The magnetic field disturbance intensity has a tendency to be underpredicted in the simulation as shown in Figure 5. The errors have a longer tail in the direction of underprediction. This indicates that for operational purposes, a sufficiently low threshold

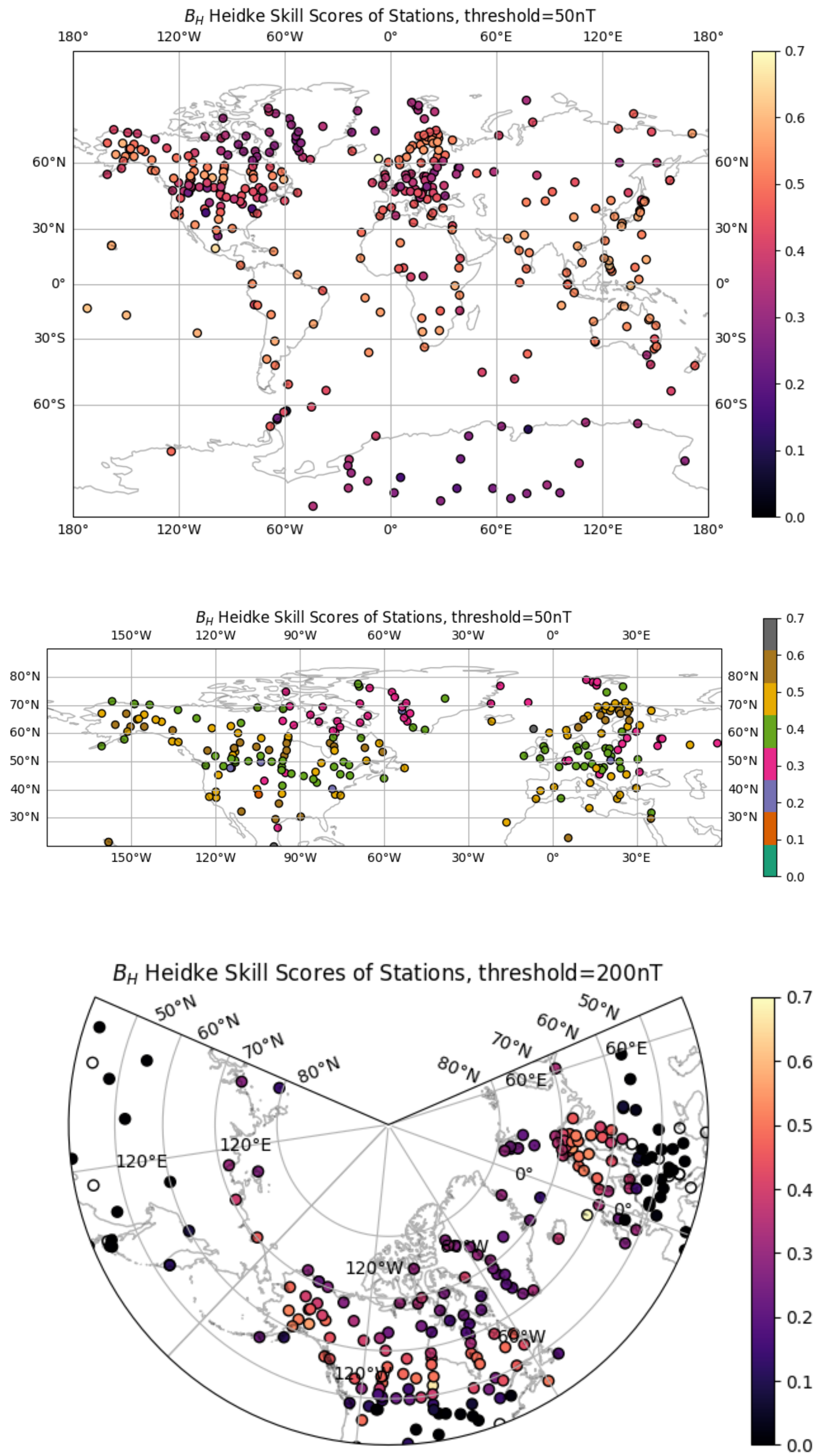

Figure 6. Station Heidke Skill Scores with a threshold of 50 nT (top and middle) and 200 nT (bottom). The top, middle, and bottom plots are in projections equal-area, equirectangular, and conic. The middle plot is in a qualitative color scheme to accentuate the change in HSS at auroral latitudes.

for event occurrence is required so that the model does not produce an overly large number of misses.

Lower-latitude stations ($-50...50°$ magnetic latitude) have generally a higher skill score than their higher latitude counterparts. This is expected, as the highly variable ionospheric currents arise from localized tail bursts, whose coupling to the ionosphere is still imperfectly modeled by the global simulations. Furthermore, the model is optimized for computing the Dst and SYM-H indices (Wanliss & Showalter, 2006; Newell & Gjerloev, 2012).

Further developing the ionospheric response and the coupled magnetotail processes offers an opportunity to improve the accuracy of the higher-latitude responses. In this study, we coupled the BATS-R-US global magnetosphere with 0.25 R_E maximum resolution to the RIM ionospheric module. Both increasing resolution of the MHD model (Welling et al., 2019) and improving the description of the conductances in the ionosphere module Mukhopadhyay et al. (2020) can influence the model accuracy and performance as measured by skill scores.

Also, as shown by A. J. Ridley et al. (2010) simulations come with inherent limitations. The RIM model is a potential solver that forces a potential between the northern and souther hemispheres. The model has a resolution of 1° latitude and 2.5° longitude. These parameters of the model must be considered. This could explain the sharp change in skill score at the auroral boundary since the potential is solved with the simplification that it is electrostatic. The currents are then derived through an empirical model as opposed to a solution through the coupling of magnetospher-ionosphere processes that result in large magnetic perturbations on the ground.

Generally, the dayside currents are largely directly driven by the solar wind while the nightside involves more processes arising from the magnetotail like the plasma sheet which complicates or makes an indirect relationship between the solar wind and the magnetosphere-ionosphere processes to simulate.

Using a similar SWMF configuration as in this study and a 2-year interval of the operational model, Liemohn et al. (2018) obtained a Heidke skill score of 0.51 for the hourly Dst index and -50 nT event threshold. It can be seen in Figure 6 that indeed stations near the equator (typically used to derive Dst) have an HSS of 0.5 or higher. It is also important to note that in the two year interval there is a lot of quiet time and our data set is biased towards storm time with moderate quiet time of 6 hours before. This still provides higher skill scores for individual stations.

The SWMF derived Dst is done in a manner similar to Yu and Ridley (2008) with the Biot-Savart law, however, without focusing on a specific station's coordinates but instead where the typical location of the ring current would be. This shows that the method in which to derive the perturbations is accurate.

Haiducek et al. (2017) studied statistics of individual storms and the global indices during those storms in January of 2005. As these are storms are not included in this study, they provide an independent comparison. They found an error probability density for SYM-H similar to the errors for mid-latitude stations shown in the bottom right panel of Figure 3. Furthermore, they also assert that increasing the simulation resolution does not necessarily improve the accuracy of SYM-H predictions.

Camporeale et al. (2020) examined statistics of individual stations, specifically regarding $\frac{dB_H}{dt}$ over a 2-year interval, focusing on three stations FRN, OTT, IQA at low, (sub-)auroral, and high latitudes. They showed that SWMF operational Geospace configuration predicts the changes in perturbation better at mid-latitudes than at high-latitudes, consistent with results in this study. Furthermore, they proposed a machine learning algorithm combined with SWMF, which was shown to increase skill scores significantly.

5 Summary and Conclusion

SWMF was capable of predicting ground magnetometer signals with a choice of 50 nT threshold in the mid-latitudes and 200 nT threshold in the high-latitudes. This leads to the posibility of using the model operationally to predict more localized phenomena such as in the auroral oval. Improvements can be made to the ionosphere model or a different ionosphere model that can simulate fine-grained localized physics. This showed the ability to predict storms that may cause GICs which is important for the high-latitude regions.

Open Research

The data set used in this research can be found at `https://deepblue.lib.umich.edu/data/concern/data_sets/g445cd54j` [pending].

The Space Weather Modeling Framework can be obtained here `https://github.com/MSTEM-QUDA/SWMF`.

Acknowledgments

The results presented in this paper rely on data collected at magnetic observatories. We thank the national institutes that support them and INTERMAGNET for promoting high standards of magnetic observatory practice (www.intermagnet.org).

We gratefully acknowledge the SuperMAG collaborators (https://supermag.jhuapl.edu/info/?page=acknowledgeme

We acknowledge use of NASA/GSFC's Space Physics Data Facility's OMNIWeb service, and OMNI data.

This research was funded by the NASA Heliophysics DRIVE Science Center (SOLSTICE) at the University of Michigan under grant NASA 80NSSC20K0600, the NSF through grant 2033563, and NASA through grant 80NSSC21K1753.

Appendix A Event list

Storms used in this study is in Table A1.

References

Abt Associates Inc. (2019, Mar). *Customer needs and requirements for space weather products and services.* Retrieved from `https://www.swpc.noaa.gov/sites/default/files/images/FINAL%20SWPC%20User%20Needs%20Report-1.pdf`

Akasofu, S.-I., Ahn, B.-H., & Kisabeth, J. (1980). Distribution of field-aligned currents and expected magnetic field perturbations resulting from auroral currents along circular orbits of satellites. *Journal of Geophysical Research: Space Physics*, *85*(A12), 6883-6887. Retrieved from `https://agupubs.onlinelibrary.wiley.com/doi/abs/10.1029/JA085iA12p06883` doi: https://doi.org/10.1029/JA085iA12p06883

Al Shidi, T., Q. Pulkkinen. (2022). *Space weather modeling framework simulations of ground magnetometer data [dataset]* [dataset]. University of Michigan - Deep Blue Data. Retrieved from `https://doi.org/10.7302/dkjd-1j05` doi: 10.7302/dkjd-1j05

Bolduc, L. (2002). Gic observations and studies in the hydro-québec power system. *Journal of Atmospheric and Solar-Terrestrial Physics*, *64*(16), 1793-1802. Retrieved from `https://www.sciencedirect.com/science/article/pii/S1364682602001281` (Space Weather Effects on Technological Systems) doi:

Table A1. List of storm onset times included in the statistical simulation study.

2010-4-5 08:27	2012-6-16 09:45	2014-4-11 05:54	2016-3-6 06:00
2010-4-11 13:10	2012-7-8 20:46	2014-5-7 23:44	2016-3-14 17:06
2010-5-2 05:38	2012-7-14 17:59	2014-6-7 16:36	2016-4-2 11:47
2010-5-28 03:08	2012-9-1 07:59	2014-8-27 03:35	2016-4-7 16:40
2010-8-3 17:13	2012-9-30 11:33	2014-9-12 15:54	2016-4-12 19:38
2010-10-11 05:41	2012-10-7 18:13	2000-1-1 00:00	2016-4-12 18:35
2011-2-14 15:37	2012-10-12 19:21	2015-2-16 19:24	2016-4-16 17:40
2011-3-1 07:05	2012-10-31 15:26	2015-3-17 04:07	2016-5-8 01:04
2011-3-9 21:41	2013-1-25 19:30	2015-4-9 21:52	2016-6-5 05:46
2011-4-6 09:27	2013-2-28 15:34	2015-4-14 12:55	2016-8-2 05:42
2011-4-11 07:05	2013-3-17 06:05	2015-5-12 18:05	2016-8-23 10:59
2011-5-28 06:23	2013-3-20 19:40	2015-5-18 10:12	2016-10-12 21:47
2011-8-5 18:02	2013-4-30 10:02	2015-6-7 10:30	2016-12-21 09:17
2011-9-9 11:52	2013-5-18 00:57	2015-6-22 05:00	2017-3-27 00:06
2011-9-17 03:31	2013-5-24 17:55	2015-7-4 13:06	2017-5-27 15:31
2011-9-26 10:00	2013-6-6 15:23	2015-7-10 22:21	2017-7-16 06:03
2011-10-24 18:20	2013-6-27 14:38	2015-7-23 01:51	2017-8-31 04:14
2012-1-22 05:38	2013-7-5 19:25	2015-8-15 08:04	2017-9-6 23:26
2012-1-24 14:49	2013-7-9 20:54	2015-8-15 07:54	2017-9-27 06:52
2012-2-18 19:41	2013-7-9 20:02	2015-8-26 05:45	2017-11-7 02:34
2012-3-7 04:36	2013-7-13 15:48	2015-9-7 13:13	2018-4-20 00:14
2012-3-8 10:29	2013-10-2 01:40	2015-9-8 21:45	2018-5-5 10:32
2012-3-12 09:10	2013-10-8 19:47	2015-9-20 05:46	2018-8-25 12:39
2012-3-15 13:38	2013-10-30 06:06	2015-10-4 00:30	2018-9-10 10:56
2012-3-15 13:14	2013-11-7 04:08	2015-10-7 01:41	2018-10-7 07:45
2012-3-27 07:25	2013-11-9 00:32	2015-11-3 05:31	2018-11-4 09:05
2012-4-4 20:48	2013-11-11 03:18	2015-11-6 18:09	2019-5-10 17:50
2012-4-23 03:09	2013-12-7 21:34	2015-11-30 06:09	2019-5-13 23:35
2012-6-2 16:37	2014-2-23 06:55	2015-12-19 16:13	2019-8-5 00:31
2012-6-10 19:39	2014-2-27 16:56	2016-2-16 06:48	2019-8-30 22:13
			2019-9-27 05:20

https://doi.org/10.1016/S1364-6826(02)00128-1

Boteler, D., Pirjola, R., & Nevanlinna, H. (1998). The effects of geomagnetic disturbances on electrical systems at the earth's surface. *Advances in Space Research*, *22*(1), 17-27. Retrieved from https://www.sciencedirect.com/science/article/pii/S027311779701096X (Solar-Terrestrial Relations: Predicting the Effects on the Near-Earth Environment) doi: https://doi.org/10.1016/S0273-1177(97)01096-X

Cai, X., & Clauer, C. R. (2013). Magnetospheric sawtooth events during the solar cycle 23. *Journal of Geophysical Research: Space Physics*, *118*(10), 6378-6388. Retrieved from https://agupubs.onlinelibrary.wiley.com/doi/abs/10.1002/2013JA018819 doi: https://doi.org/10.1002/2013JA018819

Camporeale, E., Cash, M. D., Singer, H. J., Balch, C. C., Huang, Z., & Toth, G. (2020). A gray-box model for a probabilistic estimate of regional ground magnetic perturbations: Enhancing the noaa operational geospace model with machine learning. *Journal of Geophysical Research: Space Physics*, *125*(11), e2019JA027684. Retrieved from https://agupubs.onlinelibrary.wiley.com/doi/abs/10.1029/2019JA027684 (e2019JA027684 10.1029/2019JA027684) doi: https://doi.org/10.1029/2019JA027684

Cash, M., Singer, . H., Millward, G., Toth, G., Welling, D., & Balch, C. (2018, July). NOAA SWPC's Operational Geospace Model Performance during Earth-Affecting Events. In *42nd cospar scientific assembly* (Vol. 42, p. D2.3-37-18).

Chapman, S., & Bartels, J. (1941). Geomagnetism. by s. chapman and j. bartels. 2 vols. pp. xxviii, 1049. 63s. 1940. (oxford university press). *The Mathematical Gazette*, *25*(263), 62–63. doi: 10.2307/3606494

Congress, U. S. (2020, Oct 21). Promoting research and observations of space weather to improve the forecasting of tomorrow act or the PROSWIFT act. *Public Law 116-181*. Retrieved from `https://www.congress.gov/bill/116th-congress/senate-bill/881`

Davis, T. N., & Sugiura, M. (1966). Auroral electrojet activity index ae and its universal time variations. *Journal of Geophysical Research*, *71*(3), 785–801.

Federal Emergency Management Agency. (2019, Jul). *2019 national threat and hazard identification and risk assessment (THIRA).* Retrieved from `https://www.fema.gov/sites/default/files/2020-06/fema_national-thira-overview-methodology_2019_0.pdf`

Forbes, J. M. (1981). The equatorial electrojet. *Reviews of Geophysics*, *19*(3), 469-504. Retrieved from `https://agupubs.onlinelibrary.wiley.com/doi/abs/10.1029/RG019i003p00469` doi: https://doi.org/10.1029/RG019i003p00469

Ganushkina, N. Y., Liemohn, M. W., & Dubyagin, S. (2018). Current systems in the earth's magnetosphere. *Reviews of Geophysics*, *56*(2), 309-332. Retrieved from `https://agupubs.onlinelibrary.wiley.com/doi/abs/10.1002/2017RG000590` doi: https://doi.org/10.1002/2017RG000590

Ganushkina, N. Y., Liemohn, M. W., Kubyshkina, M. V., Ilie, R., & Singer, H. J. (2010). Distortions of the magnetic field by storm-time current systems in earth's magnetosphere. *Annales Geophysicae*, *28*(1), 123–140. Retrieved from `https://angeo.copernicus.org/articles/28/123/2010/` doi: 10.5194/angeo-28-123-2010

Gjerloev, J. W. (2012). The supermag data processing technique. *Journal of Geophysical Research: Space Physics*, *117*(A9). Retrieved from `https://agupubs.onlinelibrary.wiley.com/doi/abs/10.1029/2012JA017683` doi: https://doi.org/10.1029/2012JA017683

Goddard Space Flight Center. (2021). *Omniweb plus.* Retrieved from `https://omniweb.gsfc.nasa.gov/`

Gombosi, Tamas I., Chen, Yuxi, Glocer, Alex, Huang, Zhenguang, Jia, Xianzhe, Liemohn, Michael W., . . . Zou, Shasha (2021). What sustained multi-disciplinary research can achieve: The space weather modeling framework. *J. Space Weather Space Clim.*, *11*, 42. Retrieved from `https://doi.org/10.1051/swsc/2021020` doi: 10.1051/swsc/2021020

Haiducek, J. D., Welling, D. T., Ganushkina, N. Y., Morley, S. K., & Ozturk, D. S. (2017). Swmf global magnetosphere simulations of january 2005: Geomagnetic indices and cross-polar cap potential. *Space Weather*, *15*(12), 1567-1587. Retrieved from `https://agupubs.onlinelibrary.wiley.com/doi/abs/10.1002/2017SW001695` doi: https://doi.org/10.1002/2017SW001695

Heidke, P. (1926). Berechnung des erfolges und der gute der windstarkevorhersagen im sturmwarnungsdienst. *Geogr. Ann.*, *8*, 301–349.

Huang, C.-S., Foster, J. C., Goncharenko, L. P., Reeves, G. D., Chau, J. L., Yumoto, K., & Kitamura, K. (2004). Variations of low-latitude geomagnetic fields and dst index caused by magnetospheric substorms. *Journal of Geophysical Research: Space Physics*, *109*(A5). Retrieved from `https://agupubs.onlinelibrary.wiley.com/doi/abs/10.1029/2003JA010334` doi: https://doi.org/10.1029/2003JA010334

INTERMAGNET et al. (2021). Intermagnet reference data set (irds) 2018 – definitive magnetic observatory data. *GFZ Data Services*. doi: https://doi.org/10.5880/INTERMAGNET.1991.2018

Jolliffe, I. T., & Stephenson, D. B. (2012). *Forecast verification: a practitioner's guide in atmospheric science*. John Wiley & Sons.

Klumpar, D. (1979). Relationships between auroral particle distributions and magnetic field perturbations associated with field-aligned currents. *Journal of Geophysical Research: Space Physics*, *84*(A11), 6524-6532. Retrieved from https://agupubs.onlinelibrary.wiley.com/doi/abs/10.1029/JA084iA11p06524 doi: https://doi.org/10.1029/JA084iA11p06524

Lanzerotti, L. J. (2001, January). Space weather effects on technologies. *Washington DC American Geophysical Union Geophysical Monograph Series*, *125*, 11-22. doi: 10.1029/GM125p0011

Liemohn, M., Ganushkina, N. Y., De Zeeuw, D. L., Rastaetter, L., Kuznetsova, M., Welling, D. T., … van der Holst, B. (2018). Real-time swmf at ccmc: Assessing the dst output from continuous operational simulations. *Space Weather*, *16*(10), 1583-1603. Retrieved from https://agupubs.onlinelibrary.wiley.com/doi/abs/10.1029/2018SW001953 doi: https://doi.org/9.1029/2018SW001953

Mukhopadhyay, A., Welling, D., Burleigh, M., Liemohn, M., Ridley, A., Zou, S., … Gjerloev, J. (2020). Global driving of auroral conductance - balance of sources & numerical considerations. *Earth and Space Science Open Archive*, 30. Retrieved from https://doi.org/10.1002/essoar.10503792.1 doi: 10.1002/essoar.10503792.1

Newell, P. T., & Gjerloev, J. W. (2012). Supermag-based partial ring current indices. *Journal of Geophysical Research: Space Physics*, *117*(A5). Retrieved from https://agupubs.onlinelibrary.wiley.com/doi/abs/10.1029/2012JA017586 doi: https://doi.org/10.1029/2012JA017586

Newell, P. T., Sotirelis, T., Liou, K., Meng, C.-I., & Rich, F. J. (2007). A nearly universal solar wind-magnetosphere coupling function inferred from 10 magnetospheric state variables. *Journal of Geophysical Research: Space Physics*, *112*(A1). Retrieved from https://agupubs.onlinelibrary.wiley.com/doi/abs/10.1029/2006JA012015 doi: https://doi.org/10.1029/2006JA012015

Onwumechili, C. A. (2019). *The equatorial electrojet*. Routledge.

Papitashvili, N., Bilitza, D., & King, J. (2014). Omni: a description of near-earth solar wind environment. *40th COSPAR scientific assembly*, *40*, C0–1.

Pirjola, R., Kauristie, K., Lappalainen, H., Viljanen, A., & Pulkkinen, A. (2005). Space weather risk. *Space Weather*, *3*(2). Retrieved from https://agupubs.onlinelibrary.wiley.com/doi/abs/10.1029/2004SW000112 doi: https://doi.org/10.1029/2004SW000112

Pirjola, R., Viljanen, A., Pulkkinen, A., & Amm, O. (2000). Space weather risk in power systems and pipelines. *Physics and Chemistry of the Earth, Part C: Solar, Terrestrial & Planetary Science*, *25*(4), 333-337. Retrieved from https://www.sciencedirect.com/science/article/pii/S1464191700000271 doi: https://doi.org/10.1016/S1464-1917(00)00027-1

Pulkkinen, A., Bernabeu, E., Thomson, A., Viljanen, A., Pirjola, R., Boteler, D., … MacAlester, M. (2017). Geomagnetically induced currents: Science, engineering, and applications readiness. *Space Weather*, *15*(7), 828-856. Retrieved from https://agupubs.onlinelibrary.wiley.com/doi/abs/10.1002/2016SW001501 doi: https://doi.org/10.1002/2016SW001501

Rastogi, R. G. (1989, January). The equatorial electrojet: magnetic and ionsopheric effects. *Geomatik*, *3*, 461-525.

Richmond, A. D., Kamide, Y., Akasofu, S.-I., Alcaydé, D., Blanc, M., de la Beaujardière, O., … Zaitzev, A. N. (1990). Global measures of ionospheric electrodynamic activity inferred from combined incoherent scatter radar and ground magnetometer observations. *Journal of Geophysical Research: Space Physics*, *95*(A2), 1061-1071. Retrieved from https://agupubs.onlinelibrary.wiley.com/doi/abs/10.1029/JA095iA02p01061 doi: https://doi.org/10.1029/JA095iA02p01061

Ridley, A., Deng, Y., & Toth, G. (2006). The global ionosphere–thermosphere model. *Journal of Atmospheric and Solar-Terrestrial Physics*, *68*(8), 839–864.

Ridley, A. J., Gombosi, T. I., Sokolov, I. V., Tóth, G., & Welling, D. T. (2010). Numerical considerations in simulating the global magnetosphere. *Annales Geophysicae*, *28*(8), 1589–1614. Retrieved from https://angeo.copernicus.org/articles/28/1589/2010/ doi: 10.5194/angeo-28-1589-2010

Ridley, A. J., & Kihn, E. A. (2004). Polar cap index comparisons with amie cross polar cap potential, electric field, and polar cap area. *Geophysical Research Letters*, *31*(7). Retrieved from https://agupubs.onlinelibrary.wiley.com/doi/abs/10.1029/2003GL019113 doi: https://doi.org/10.1029/2003GL019113

Siscoe, G. L., & Crooker, N. U. (1974). On the partial ring current contribution to dst. *Journal of Geophysical Research*, *79*(7), 1110–1112.

Space Weather Prediction Center. (1960). *Geospace ground magnetic perturbation maps.* Retrieved from https://www.swpc.noaa.gov/products/geospace-ground-magnetic-perturbation-maps

Sugiura, M., & Poros, D. (1971). *Hourly values of equatorial dst for the years 1957 to 1970.* NASA, Goddard Space Flight Center.

Tóth, G., van der Holst, B., Sokolov, I. V., De Zeeuw, D. L., Gombosi, T. I., Fang, F., … Opher, M. (2012). Adaptive numerical algorithms in space weather modeling. *Journal of Computational Physics*, *231*(3), 870-903. Retrieved from https://www.sciencedirect.com/science/article/pii/S002199911100088X (Special Issue: Computational Plasma Physics) doi: https://doi.org/10.1016/j.jcp.2011.02.006

Vasyliunas, V. M. (1970). Mathematical models of magnetospheric convection and its coupling to the ionosphere. In *Particles and fields in the magnetosphere* (pp. 60–71). Springer.

Villante, U., & Piersanti, M. (2008). An analysis of sudden impulses at geosynchronous orbit. *Journal of Geophysical Research: Space Physics*, *113*(A8). Retrieved from https://agupubs.onlinelibrary.wiley.com/doi/abs/10.1029/2008JA013028 doi: https://doi.org/10.1029/2008JA013028

Wanliss, J. A., & Showalter, K. M. (2006). High-resolution global storm index: Dst versus sym-h. *Journal of Geophysical Research: Space Physics*, *111*(A2). Retrieved from https://agupubs.onlinelibrary.wiley.com/doi/abs/10.1029/2005JA011034 doi: https://doi.org/10.1029/2005JA011034

Waters, C. L., Anderson, B. J., & Liou, K. (2001). Estimation of global field aligned currents using the iridium® system magnetometer data. *Geophysical Research Letters*, *28*(11), 2165-2168. Retrieved from https://agupubs.onlinelibrary.wiley.com/doi/abs/10.1029/2000GL012725 doi: https://doi.org/10.1029/2000GL012725

Welling, D. T., Dimmock, A. P., Rosenqvist, L., Morley, S., & Yordanova, E. (2019, December). Resolving small scale GIC effects: What is our capability? In *Agu fall meeting abstracts* (Vol. 2019, p. SH32B-05).

Yu, Y., & Ridley, A. J. (2008). Validation of the space weather modeling framework using ground-based magnetometers. *Space Weather*, *6*(5). Retrieved from https://agupubs.onlinelibrary.wiley.com/doi/abs/10.1029/2007SW000345 doi: https://doi.org/10.1029/2007SW000345

Zheng, K., Trichtchenko, L., Pirjola, R., & Liu, L.-G. (2013). Effects of geophysical parameters on gic illustrated by benchmark network modeling. *IEEE Transactions on Power Delivery*, *28*(2), 1183-1191. doi: 10.1109/TPWRD.2013.2249119

Zmuda, A. J., & Armstrong, J. C. (1974, June). The diurnal variation of the region with vector magnetic field changes associated with field-aligned currents. *J. Geophys. Res.*, *79*(16), 2501-2502. doi: 10.1029/JA079i016p02501